

A Spatially Selective Approach to Doppler Estimation for Frame-Based Satellite SAR Processing

Ian G. Cumming, *Member, IEEE*

Abstract—When Doppler centroid estimators are applied to satellite synthetic aperture radar (SAR) data, biased estimates are often obtained because of anomalies in the received data. Typical anomalies include areas of low SNR, strong discrete targets, and radiometric discontinuities. In this paper, a new method of Doppler centroid estimation is presented that takes advantage of principles such as spatial diversity, estimator quality checks, geometric models, and the fitting of a “global” estimate over a wide area of a SAR scene. In the proposed scheme, Doppler estimates are made over small blocks of data covering a whole frame, so that all parts of the scene are potentially represented. The quality of each block estimate is examined using data statistics or estimator quality measures. Poor estimates are rejected, and the remaining estimates are used to fit a surface model of the Doppler centroid versus the range and azimuth extent of the scene. A physical model that relates the satellite’s orbit, attitude, and beam-pointing-direction to the Doppler centroid is used to get realistic surface fits and to reduce the complexity (dimensionality) of the estimation problem. The method is tested with RADARSAT-1 and Shuttle Radar Topography Mission X-band SAR (SRTM/X-SAR) spaceborne data and is found to work well with scenes that do have radiometric anomalies, and in scenes where attitude adjustments cause the Doppler to change rapidly.

Index Terms—Geometry models, global surface fit, quality metrics, satellite synthetic aperture radar (SAR) Doppler centroid estimation.

I. INTRODUCTION

AN ESSENTIAL PART of SAR processing is the estimation of the Doppler centroid frequency of the received data [1]–[4]. Despite many advances in SAR processing and data handling in general, most production SAR processing systems for satellite SAR data suffer from unreliable Doppler centroid estimates in about 2% to 5% of the scenes processed. Poor estimates raise the noise and ambiguity levels in the processed image, sometimes to the point of seriously affecting image clarity [5]. ScanSAR data are more affected than regular-beam data, because the centroid is harder to estimate, yet its accuracy requirements are more demanding [6].

The Doppler centroid is difficult to estimate accurately because: 1) the satellite system does not have sufficiently accurate attitude measurements or beam-pointing knowledge to calculate the centroid from geometry alone; 2) the received data have local anomalies that upset the estimation process [7], [8]. In this

paper, an integrated approach is taken to improve the estimation accuracy, involving the following four concepts.

- 1) The concept of “spatial diversity” is used, in which Doppler estimates are obtained from widely spread areas of the scene, rather than from concentrated areas such as the beginning of the scene.
- 2) Quality measurements are used to identify and reject those parts of the received data that create the main estimation anomalies.
- 3) A geometric model is incorporated that can compute a Doppler surface given the satellite attitude values during the data acquisition of the scene.
- 4) A “global” model-based fitting procedure is used that fits a Doppler centroid surface over a whole frame of data in one operation.

Most of these concepts are not new, as some have been used previously in a number of processors. However, it is believed that the incorporation of quality measures and the integrated approach represents a more robust solution to the Doppler estimation problem.

The geometric model has the advantage of reducing the dimensionality of the estimation problem, and of imposing a physical reality on the answer. Shuttle Radar Topography Mission X-band SAR (SRTM/X-SAR) and RADARSAT data are used to illustrate the operation of the new estimation algorithm, and to predict its accuracy. Results to date indicate the Doppler centroid estimation accuracy can be 5 Hz or better with difficult scenes, which is accurate enough to allow high image quality in the processed SAR images.

There have been many approaches taken for Doppler centroid estimation, as evidenced by the references cited. One of the most comprehensive approaches taken to date is represented by the work of Dragošević, in which geometry models and along-track filters are used over long scenes [9], [10]. Our method has some similarities with her method, and some differences, notably the use of small blocks, quality checks and rejection of blocks. Our approach is optimized for estimators working on one frame of data at a time, as in processors with randomly ordered production orders, while her approach with Kalman filters is optimized for strip-mode processing.

In this paper, the concepts of spatial diversity, block estimates and estimator quality measures are introduced in Section II. The surface fitting approach is presented in Section III, where either a polynomial or an attitude/geometry model can be used. Details of the geometry model are presented in Section IV, where examples of Doppler calculations are given. Details of the automatic surface fitting approach are given in Section V, and examples using RADARSAT and X-SAR data are presented in Section VI.

Manuscript received June 12, 2003; revised November 13, 2003. This work was supported by the MacDonald Dettwiler/NSERC Industrial Research Chair in Radar Remote Sensing.

The author is with the Department of Electrical and Computer Engineering, The University of British Columbia, Vancouver, BC, Canada V6T 1Z4 (e-mail: ianc@ece.ubc.ca).

Digital Object Identifier 10.1109/TGRS.2004.825577

II. PRINCIPLES OF THE GLOBAL ESTIMATION PROCEDURE

In this section, three of the main concepts that are used in developing the new Doppler estimator are presented. These include the concept of spatial diversity, the use of image blocks to obtain the diversity, and the measurement of parameters that predict the accuracy of each block. The fourth concept of a global fitting procedure is presented in Section III.

A. Spatial Diversity Using Blocks

The concept of “spatial diversity” refers to the use of data from representative parts of the radar scene in the estimation process. When scenes are large, it may not be feasible to use all the data, but it is important to spread out the data sources so all representative parts of the scene are included. However, choices can be made so that parts of a radar scene which provide good Doppler estimates can be included, while other parts that provide noisy or biased estimates are excluded.

Poor estimates arise primarily from areas of the scene where the backscatter is very weak (the received SNR is low), from areas where strong discrete targets are present, and from areas where the received energy is changing abruptly. The low SNR areas raise the standard deviation of the block estimates, and the strong targets and the varying radiometry can introduce large biases into the block estimates, mainly because of the partially captured Doppler history [7].

In some SAR processors, a group of range lines at the beginning of each processed frame are used to form the Doppler estimate. This approach can inadvertently use areas of the scene that bias the estimator and miss the azimuth dependence of the Doppler. To avoid the bad areas, a “spatial diversity” approach is proposed. In this approach, the whole scene is divided up into blocks or subscenes, the primary estimators are applied to each block separately, and only blocks that provide reliable answers are included in the global estimation procedure. The larger the scene, the better this approach works.

The spatial distribution of blocks can be sparse, contiguous or overlapping, depending upon the scene size and the computing resources available. In the present work, contiguous blocks are used, with a size of 256×1024 samples (range \times azimuth), which represent about 5×5 km of ground coverage for typical C-band satellite SARs. This size is approximately the extent of the instantaneous beam footprint, and provides a good compromise between block independence and estimate redundancy when the blocks are contiguous.

Block Estimates: There are many Doppler estimation approaches that can be used on the blocks. Both the baseband [fractional pulse repetition frequency (PRF)] and ambiguity (integer PRF) parts of the centroid must be estimated, and different algorithms are used for each part [11]–[14]. It is found that the choice of algorithm used to obtain the baseband part is not very critical, as most methods are reliable (e.g., Madsen’s method [8]). But for the ambiguity estimate, it is very important to choose a robust algorithm. In fact, it is recommended that several ambiguity algorithms be used for a given block, as their performance is quite dependent upon the scene content.

In most SAR systems, the antenna is unweighted in azimuth, yielding a sinc-squared pattern. However, receiver noise tends

to fill in the valleys of the pattern, giving rise to an azimuth spectrum that is roughly shaped like a sine wave. For RADARSAT data, the present experiments showed that a sine wave on a pedestal is a good model for the averaged azimuth magnitude spectrum, when the scene radiometry is reasonably uniform. Under these conditions, a suitable model for the baseband azimuth spectrum is given by

$$S_{\text{bb}}(f) = S_0 + 2\text{Re}\{S_1\} \cos\left(\frac{2\pi f}{F_a}\right) + 2\text{Im}\{S_1\} \sin\left(\frac{2\pi f}{F_a}\right), \quad 0 \leq f < F_a \quad (1)$$

where F_a is the PRF and S_0 , and S_1 are the first two discrete Fourier transform or discrete Fourier series coefficients of the magnitude spectrum of the received data. Then, the estimate of the baseband part of the Doppler centroid frequency is obtained simply from

$$F_{\text{bb}} = \frac{\text{angle}\{S_1\}}{2\pi} F_a \quad (2)$$

One has to be more careful in estimating the Doppler ambiguity. The phase increment, wavelength diversity method introduced by the German Aerospace Center (DLR) [15], and the multilook cross-correlation (MLCC) and multilook beat frequency (MLBF) methods developed by MacDonald Dettwiler [16] are found to provide the most reliable ambiguity estimates on many scenes that have been tested. Taken individually, these methods do not work well on all scenes. But as the DLR/MLCC methods work best on low-contrast areas, and the MLBF method works best on high-contrast areas, a good strategy is to use both algorithms and select the most reliable answer for each area based upon quality measures.

For ScanSAR data, the PRF diversity method of ambiguity estimation is likely the wisest choice, as it can be applied to the part of the scene where the beams overlap, as long as the PRF differences or ambiguity numbers are high enough [10], [17].

B. Estimator Quality Measures

When the Doppler estimates are obtained for each block, quality measures are used to estimate their accuracy, and to serve as a basis to remove offending blocks from the estimation procedure. Some quality measures can be computed from the radar data itself, and some obtained from statistical analysis of the estimation results.

In the case of the input radar data, it is useful to examine the energy levels, the contrast, and the radiometric gradients in each block of the scene. The *contrast* is measured using

$$C = \frac{E\{|P_{i,j}|^2\}}{E\{|P_{i,j}|\}^2} \quad (3)$$

where $|P_{i,j}|$ is the pixel magnitude of the range-compressed data. The *gradients* are found by dividing each 5-km block into 4×4 subblocks, measuring the energy in each subblock, and finding the average slope of the energy in the range and azimuth directions for each block. High azimuth gradients are used to reject blocks for both the baseband and the ambiguity estimators, and contrast is used to select between the DLR/MLCC and MLBF ambiguity estimators. The range gradient tends not to

bias the estimators because range compression localizes the radiometric effects.

While the SNR can be estimated from the input data, it is found that it can be effectively measured by proxy using the magnitude ratio between the S_1 and S_0 terms in (1). This is convenient, when S_1 and S_0 are obtained during the baseband estimation procedure. The resulting ‘‘Harmonic ratio’’ is defined as

$$H_{\text{ratio}} = 20 \log_{10} \left(\frac{\text{abs}(S_1)}{\text{abs}(S_0)} \right). \quad (4)$$

Poor SNR is indicated by low values of this ratio.

It is also useful to measure the *distortion* of the received spectrum compared with the expected spectrum. Estimation biases arise mainly from asymmetry in the received spectrum, which can be effectively measured by the rms deviation between the averaged spectra and the fitted curve (1). The rms deviation is divided by the average height of the spectrum and multiplied by 100 to express the deviation as a percentage.

Very low SNR, very high SNR, high azimuth radiometric gradients and high spectral distortion are the main criteria used to reject baseband Doppler estimates using the quality measures. There is some correlation between these variables, but they each contain some independent information. The local standard deviation of block estimates is also a useful quality measure. Scatter plots can be used to assess the utility of the various quality measures, as seen in the examples in Section VI-B.

The DLR/MLCC Doppler ambiguity estimators use average phase increments from one range line to the next to obtain estimates of the absolute Doppler centroid [15], [16]. The phase increments are measured from the azimuth correlation coefficient at lag 1, averaged over range, as in [8]. The best quality measure is found to be the standard deviation of these average phase increments. The MLBF estimator works by finding the frequency of the strongest discrete signal when the azimuth signals of two range looks are multiplied [16]. It is found that the best quality measure is the ratio between the peak energy and the surrounding spectral energy. The quality measures used for the baseband estimates are also useful for the ambiguity estimates.

By examining scatter plots of the quality parameters for a number of scenes, appropriate thresholds for the quality parameters can be found. By setting conservative thresholds, scene-independent values emerge and can be used to set the initial rejection mask. This mask is used in the automatic surface fitting procedure discussed in Section V.

III. SURFACE FITTING APPROACHES

The objective of the surface fitting approach is to stand back and take a global view, estimating the Doppler centroid frequency over the whole processed scene in an integrated procedure. To illustrate the approach, consider baseband Doppler estimates of the RADARSAT-1 scene shown in Fig. 1.

The baseband estimates taken from the individual 5-km blocks of the scene are shown in Fig. 11. The variability of the estimates is clearly seen, especially along the shorelines. As the satellite attitude changes slowly, and the antenna pattern



Fig. 1. RADARSAT-1 S7 scene of the St. Lawrence River and Anticosti Island.

is a smooth function of range, the Doppler centroid cannot take jumps like the ones shown. Therefore, the *true* Doppler frequency is a *smooth function* of range and azimuth, as is found in the final estimates in Fig. 16. By comparing Fig. 11 with Fig. 16, it becomes clear that a good overall estimate can be obtained if the biased and noisy blocks of Fig. 11 can be removed from the estimation procedure. This illustrates the importance of taking the *spatially selective global view* when estimating the Doppler centroid.

A. Global Fit Using a Polynomial Surface

After obtaining the fractional PRF and ambiguity estimates for each block in the scene and rejecting the bad estimates, a two-dimensional (2-D) surface of Doppler centroid versus range and azimuth is fitted. The simple approach of fitting a low-order polynomial surface

$$F_{\text{bb}}(r_i, a_i) = c_0 + c_{a1}a_i + c_{r1}r_i + c_{r2}r_i^2 + c_{ar}a_i r_i + c_{a2}a_i^2 + c_{r3}r_i^3 \quad (5)$$

to the unwrapped block estimates is first investigated, where r_i and a_i are the range and azimuth block numbers relative to the scene center.¹

The coefficient c_0 is the average Doppler frequency over the whole scene. The coefficient c_{r1} accounts for most of the sizable variation of Doppler with range, and c_{r2} and c_{r3} allow small quadratic and cubic components in the range variation. Normally, a linear term c_{a1} is sufficient to model a slowly varying azimuth drift in the Doppler centroid over 100 or 200 km, but a quadratic component c_{a2} is useful to follow the faster Doppler changes caused by the frequent firing of the attitude thrusters in the SRTM case. Finally, a cross-coupling term c_{ar} is introduced to model a range slope that changes with azimuth, as happens as the satellite latitude changes or the antenna yaw angle drifts.

¹Absolute block numbers are used in the annotation of all the figures for convenience.

A Nelder–Mead simplex direct search method is used to estimate the coefficients in (5) [18].² The geometry model of Section III-B is used to provide the initial values of the coefficients, assuming a zero or nominal satellite attitude. In fact, some of the smaller terms, such as c_{r2} and c_{r3} , are relatively independent of attitude and can be set directly from the zero-attitude geometry model.

Separate procedures are usually applied to obtain the fractional PRF surface fit and ambiguity estimate. In principle, a single fitting procedure can be applied to obtain the polynomial surface fit to the *absolute* Doppler estimates. However, advantage can be taken of the fact that the ambiguity is an integer, and a single ambiguity number applies to the whole scene once PRF wraparounds have been removed from the fractional estimates.

The method described has been developed for frame-based SAR processors. If the SAR data are to be processed in a long continuous strip, better results can be obtained if the Doppler centroid is updated as each new group of range lines is processed. The spatial diversity approach can be used on blocks representing the new range lines, and a Kalman filter can be used to update the surface fit [19]. A model-based filtering approach has been successfully used for long strips of ScanSAR data [10].

B. Global Fit Using a Geometry Model

The Doppler centroid frequency can be computed for a given satellite orbit and attitude angle of the radar antenna [20]. In our approach, this is accomplished by transforming the antenna pointing angle into the fixed earth-centered inertial (ECI) frame of reference and solving for the coordinates of points on the earth's surface lying along the beam centerline. Representative "targets" are selected on the beam centerline, and the Doppler centroid is calculated from the dot product of the satellite–target relative velocity vector and the unit beam look direction, scaled by $\lambda/2$, as described in Section IV.

Next, attitude and attitude rate constraints are applied, which are $\pm 0.5^\circ$ and $\pm 0.01^\circ/\text{s}$, respectively, in the case of RADARSAT-1. From these limits, extreme values of the coefficients (5) are deduced and used to limit the parameter search procedure.

Another approach uses the physical geometry model in a more direct way, in which the Doppler frequency is expressed explicitly as a function of attitude and its derivatives

$$F_{bb}(r_i, a_i) = F_{za}(r_i, a_i) + \Delta \mathcal{F}(\phi, \phi', \phi'', \psi, \psi', \psi'') \quad (6)$$

where ϕ is the yaw angle, ψ is the pitch angle, and the primes denote time derivatives. The term $F_{za}(r_i, a_i)$ is the zero-attitude component of the Doppler centroid, which can be precomputed from the orbit data. If the satellite is yaw steered, such as the European Remote Sensing (ERS) or Environmental Satellite (ENVISAT), the centroid lies mainly within the baseband, so $F_{za}(r_i, a_i)$ is near zero and can be omitted from (6)—small biases in the yaw steering can be absorbed into the yaw and pitch estimates. The range dependence of $F_{bb}(r_i, a_i)$ is given by the

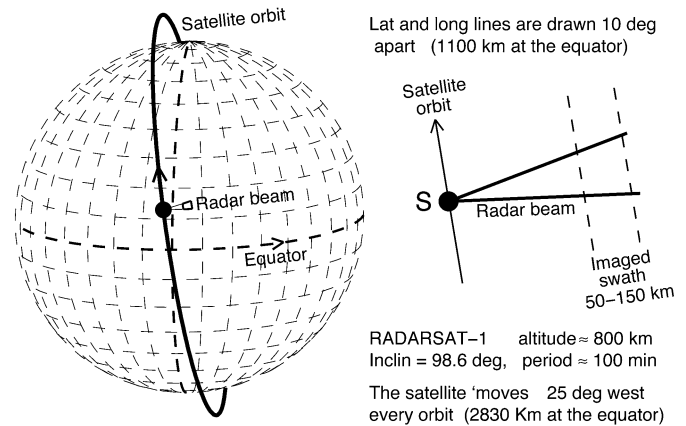


Fig. 2. Sketch of the satellite orbit and the radar beam.

beam geometry, while the azimuth dependence is given mainly by the change in the earth's rotation component and the attitude rates.

The search procedure is applied directly to the attitude parameters on the right-hand side of (6), and the attitude and rate limits are applied to the search space. If the satellite is not under maneuver, the second derivative terms can be omitted. As the effects of yaw and pitch on the Doppler centroid are quite cross-coupled, it is helpful to make the parameter space orthogonal before applying the optimization algorithm.

Both the polynomial model (5) and the direct geometry model (6) work well in the surface fitting procedure. The polynomial model is simpler to program, as a simple geometry model can be used for the constraints. It also provides an expression for the centroid in a form that is simple to use in the SAR processor. The direct geometry model has the advantage that it provides a more physical interpretation for the results, and physical constraints can be directly applied. The geometry model and the surface fitting procedure are discussed in the next two sections.

IV. GEOMETRY MODELS FOR THE DOPPLER CENTROID

This section shows how the Doppler centroid can be calculated from a geometry model, given the satellite orbit, the satellite attitude, and the pointing direction of the radar beam.

A. Satellite/Earth Geometry

The geometry model begins with a description of the satellite orbit, as sketched in Fig. 2. The satellite orbit is usually described by orbital elements or by state vectors [21], but for illustration purposes, a circular orbit is assumed in this paper [22]. The RADARSAT-1 satellite is used as an example—it has an average height above the surface of 800 km and an inclination of 98.6° .

B. Radar Beam Geometry

Next, the beam-pointing direction must be specified. This requires the knowledge of the satellite attitude, the local vertical, plus the beam nadir angle corresponding to the slant range being observed. As roll angle has little effect on the Doppler centroid, only pitch and yaw are used to specify the beam angle. Pitch and

²A Newton–Raphson steepest descent method can be used to provide faster convergence.

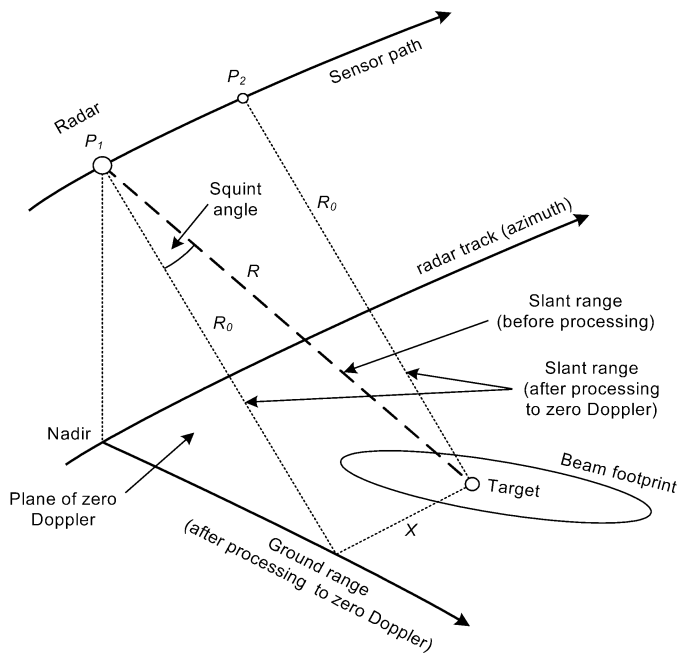


Fig. 3. Oblique view of the satellite path and the footprint of the radar beam.

yaw rates and accelerations are used to follow the Doppler centroid along track. A sketch of the geometry of the radar beam and how it intersects the earth's surface is shown in Fig. 3.

The problem is to determine the Doppler frequency along the beam center line using a geometry model, which includes how the Doppler is affected by satellite yaw and pitch. To do this, the relative velocity between the sensor and a target on the earth's surface must be computed. The relative velocity varies around the orbit, because of the earth's surface velocity changing with latitude and the varying angle between the satellite and target's velocity vectors.

C. Calculation of Doppler Frequency

The next step is to calculate the Doppler centroid frequency from the relative velocity, for arbitrary points around the orbit and for arbitrary beam-pointing angles. First, a one-dimensional (1-D) solution is obtained, whereby a plot of Doppler frequency versus beam nadir angle is computed at a given satellite position.

A flowchart of the calculation procedure is shown in Fig. 4. After specifying the satellite orbit and an array of beam elevation angles (Step 1), the time in orbit is selected, and the satellite yaw and pitch are specified (Step 2). For each beam nadir angle (Step 3), the intersection of the beam with the WGS-84 surface is computed, defining the target position along the beam center line (Step 4). If terrain height is available, it can be included at this point. Next, the range from the satellite to the target, the target velocity and the satellite velocity are calculated in the same frame of reference, and the Doppler frequency of the target is calculated from the relative velocities (Step 5). When the Doppler frequency is found for all nadir angles, a polynomial can be fitted to the curve of Doppler frequency versus slant range (Step 6).

By varying the time parameter, the 1-D Doppler "line" can be expanded into a 2-D Doppler "surface," which is the focus of

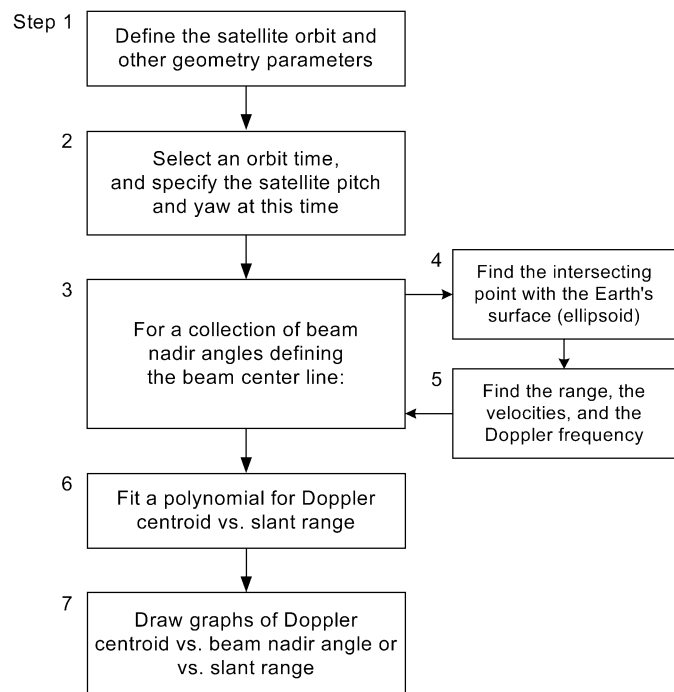


Fig. 4. Steps in computing a 1-D model of Doppler centroid frequency versus range.

this paper. The benefit of this geometric approach is that it gives a physically plausible structure to the Doppler surface, assuming that realistic attitude and attitude rate parameters are selected. By this method, unrealistic Doppler surfaces are excluded, and a smooth surface of Doppler versus range and azimuth is obtained.

A flowchart of the Doppler frequency calculation is given in Fig. 5, and the mathematical details are given in the Appendix. The procedure consists of a sequence of coordinate rotations to get the radar beam's "view vector" into ECI coordinates. Then, a quadratic equation is solved to find the point where the beam intersects the earth's surface (defining the target location), and the target's position and velocity are rotated into ECI coordinates. The solution can also be obtained in earth-centered rotating (ECR) coordinates. With both the satellite and target positions and velocities expressed in the same coordinate system, the calculation of Doppler frequency follows from

$$F_d = \frac{2V_{\text{rel}}}{\lambda} \quad (7)$$

where V_{rel} is the difference between the satellite and target's velocities, after each is projected upon the beam view vector.

D. Examples of Doppler Calculations

With this geometry model, the Doppler centroid can be calculated for a variety of SAR imaging conditions. For example, for a fixed beam nadir angle and zero satellite attitude, the Doppler centroid around the whole orbit can be found. This gives the azimuth dependence of the $F_{za}(r_i, a_i)$ term in (6). Such an example is shown in Fig. 6, for beam nadir angles of 16° , 32° , and 52° . Note that the Doppler centroid reaches a maximum of 14 300 Hz at the equator, representing about 11 ambiguities at a PRF of 1300 Hz. The small asymmetry in the curves is due to

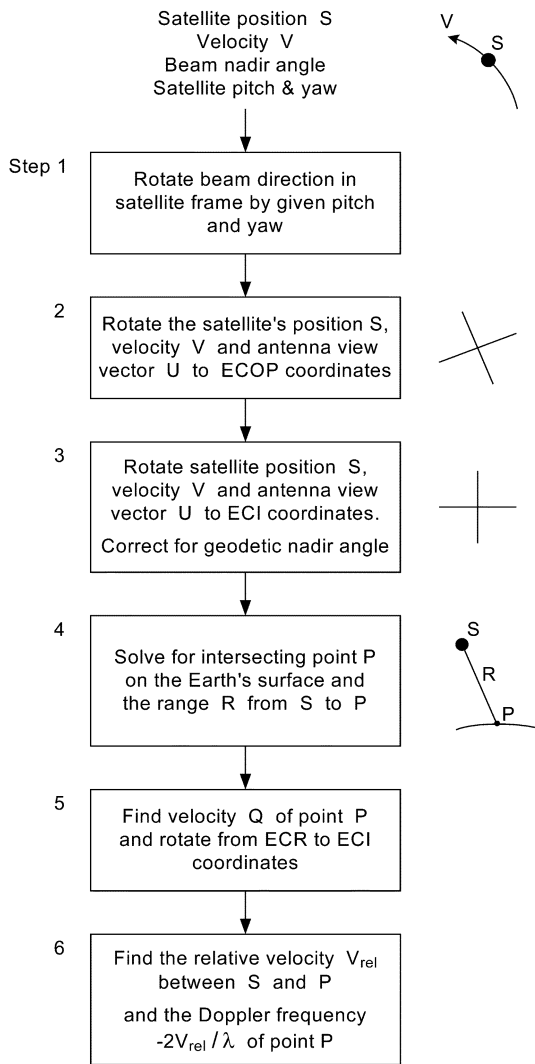


Fig. 5. Details of the Doppler frequency calculation from geometry.

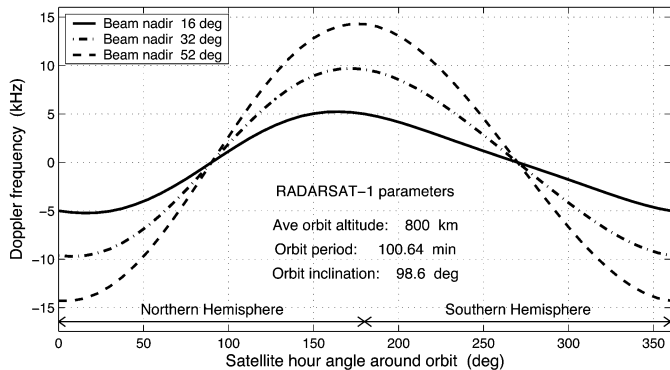


Fig. 6. Doppler centroid frequency of RADARSAT a round the orbit for three beam nadir angles.

the satellite attitude being referenced to the local vertical rather than the earth's center.

The Doppler centroid can be plotted versus slant range, as illustrated in Fig. 7. The plot covers the second quarter of the orbit in ten steps, starting from the most northerly point of the orbit

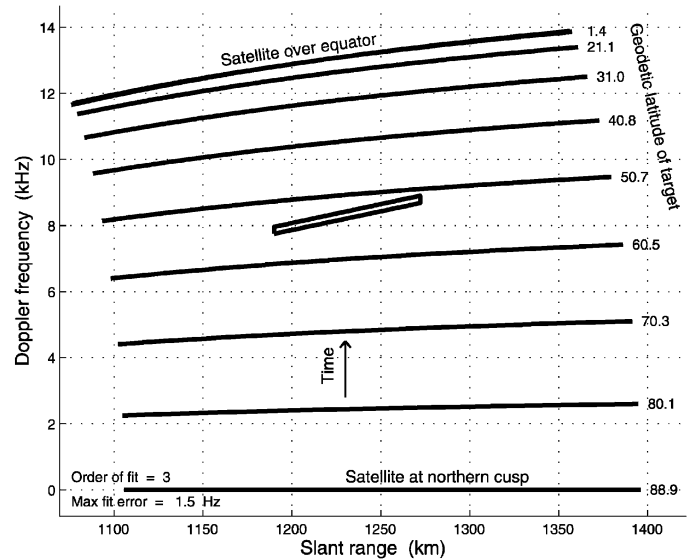


Fig. 7. Doppler frequency versus slant range for various satellite positions over the second quarter of the orbit (descending pass). The satellite attitude is zero and the beam nadir angle limits are the same for each curve. The target latitude at far range is annotated at the end of each line. The thin parallelogram delineates the Doppler-range extent of the RADARSAT example discussed in Section VI.

and ending at the descending node crossing (follow the plots from the bottom to the top in the figure). The Doppler centroid is zero when the satellite is at its most northerly or southerly point in the orbit, when the velocity vectors are parallel. The Doppler centroid is a maximum when the target is on the equator, where its velocity is highest.

A cubic polynomial is fitted to each Doppler line, which gives the c_0 , c_{r1} , c_{r2} , and c_{r3} terms in (5) at each orbit position. The polynomial fits the geometry model to within 1.5 Hz over the range swath, which justifies the use of the polynomial form of the surface fit of (5).

In another application of the model, the attitude angle needed for yaw steering to zero Doppler can be found. For example, when the satellite is over the equator, a yaw value of -3.93° is needed to steer RADARSAT's beam to the zero Doppler line.

V. AUTOMATIC FITTING PROCEDURE

The Doppler calculations using the geometry model can be embedded in an automatic fitting procedure, as shown in Fig. 8. Once the individual block estimates $F_{d_measured}(r_i, a_j)$ and their quality measures are available, the objective is to find the best fit over the whole scene of the surface: $F_{d_modeled}(r_i, a_i, \phi, \phi', \phi'', \psi, \psi', \psi'')$.

The procedure begins by dividing the scene into blocks and estimating the baseband component F_{bb} of the Doppler centroid for each block. The baseband estimates often extend around a PRF boundary, as is the case when the ambiguity number changes within a scene. In this case, the baseband estimates must be unwrapped in range and in azimuth. No unwrapping errors were found in the examples studied. Such errors are not expected to be a problem, as the ambiguity changes across range in a smooth way, as predicted by the Doppler frequency versus range curve available from the zero-attitude geometry model.

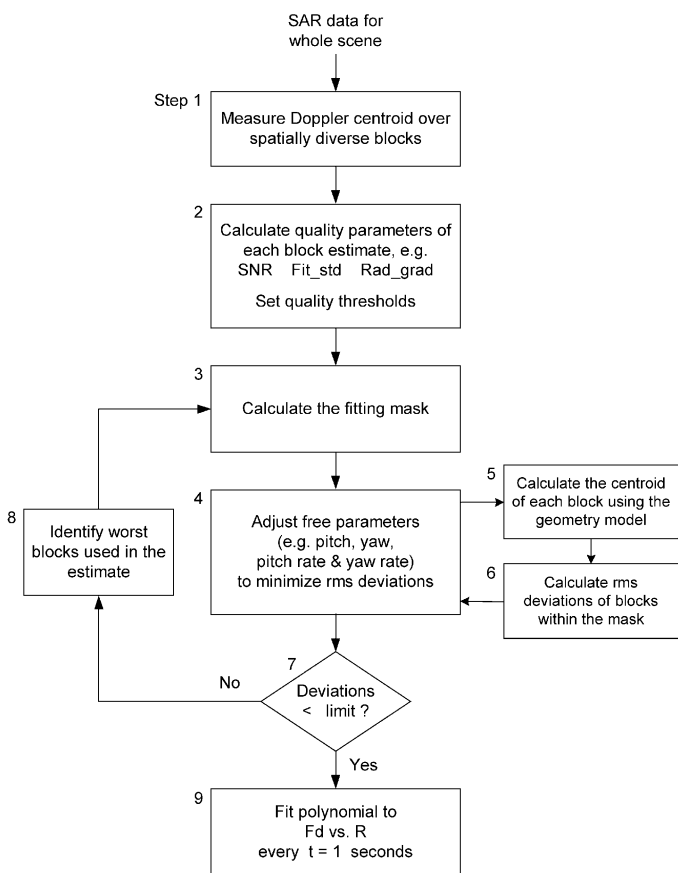


Fig. 8. Flowchart of automatic Doppler centroid surface fitting procedure.

The ambiguity number M_{amb} of the scene can be estimated at this stage [15], [16], as the geometry model inherently works with the absolute Doppler estimates

$$F_{d_measured}(r_i, a_i) = F_{bb_measured}(r_i, a_i) + M_{amb} PRF. \quad (8)$$

In Step 2, the quality parameters are calculated, and thresholds of the block rejection criteria are set. The data SNR, the spectral fit standard deviation and the azimuth radiometric gradient can be used effectively to determine the quality of the baseband estimates. In Step 3, a fitting mask is calculated, which indicates the block estimates that satisfy the initial quality thresholds, and that are used in the first iteration of the surface fit.

Steps 4–6 constitute an iterative fitting procedure, whereby the free parameters of the model are adjusted using a search procedure, to minimize the rms deviations between the model and the measured block frequencies. Normally, the pitch and yaw and their rates are used in the model, but the second derivatives can also be used if a satellite attitude maneuver is anticipated. In Step 5, the geometry model of Fig. 5 is used to calculate the Doppler centroid frequency of each block, using the procedure outlined in Section IV-C. Only those blocks within the mask are used to find the rms deviation between the surface fit and the block estimates in Step 6.

Step 7 controls the iteration termination criteria. Normally, the size of the rms deviations provide a practical termination metric. However, there are cases where the rms deviations do not converge smoothly, and other criteria are brought into play.

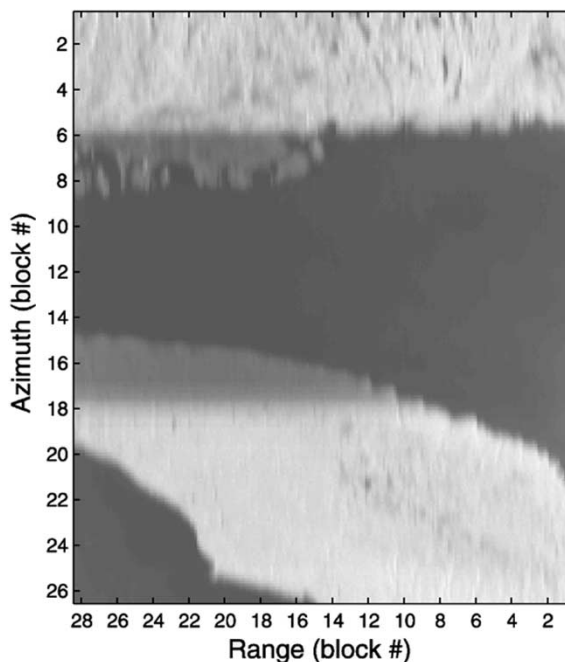


Fig. 9. Range-compressed intensity of the Anticosti scene. The annotation indicates the center of each block used in the estimator.

These include a maximum number of iterations, a leveling out of the rms deviations, a minimum percentage of blocks or a minimum degree of spatial diversity retained in the mask. The most serious case occurs when the “bad” blocks are concentrated along one edge of the image, which tends to “tilt” the estimated surface. In this case, the spatial diversity criteria is imposed to ensure that a minimum number of blocks is retained within specific subareas of the scene. This problem tends to go away as scenes become larger, suggesting that the method will work well for ScanSAR scenes.

If the iterations proceed to Step 8, the block or group of blocks having the largest deviation can be removed from the fitting mask, subject to the spatial diversity constraints. If the iterations are terminated, the results are converted to a form needed by the SAR processor, such as a polynomial of Doppler centroid versus range computed every second of azimuth time. Goodness-of-fit parameters are also computed in Step 9.

VI. RESULTS WITH RADARSAT DATA

The surface-fitting procedure is best illustrated by tracing through the results of a scene that has experienced Doppler estimation errors in a production processor. For this purpose, a RADARSAT-1 Beam S7 descending-orbit scene with prominent land–sea boundaries is used. The 114×136 km scene is shown in Fig. 1, acquired from orbit 2842 on May 22, 1996. The scene center is at 49.95° North latitude and 63.09° West longitude. The platform heading is 196° , so that the top of the image is oriented about 16° east of north. The PRF is 1286.25 Hz and the sampling rate is 12.927 MHz. The scene includes the St. Lawrence River in Eastern Canada, with two bodies of land—Anticosti Island is in the lower part of the image, and the mainland of the Province of Quebec is in the upper part.

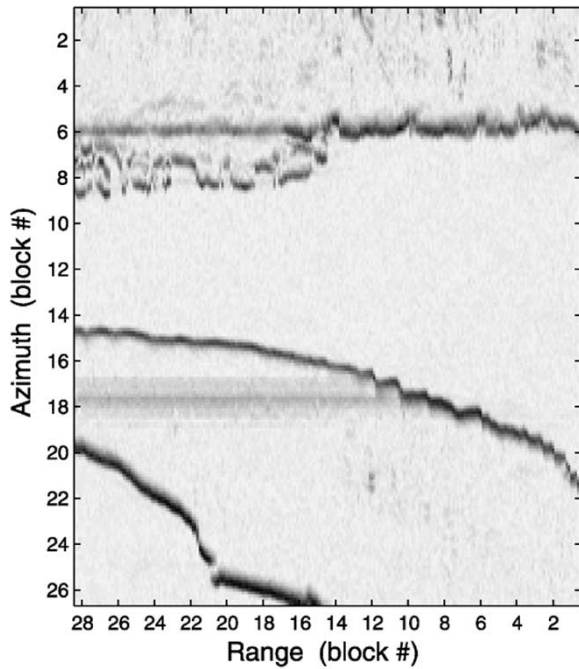


Fig. 10. Azimuth radiometric gradient of the Anticosti scene.

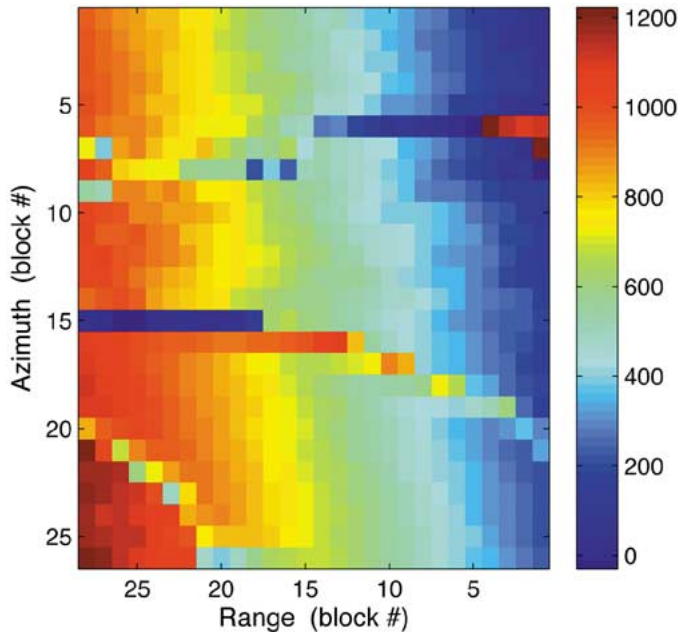


Fig. 11. Baseband Doppler centroid estimates F_{bb} taken over contiguous 5-km blocks of the Fig. 1 scene (hertz).

The data used for the Doppler estimation experiments are shown in Fig. 9. The image shown is not well focused, as range cell migration correction and azimuth compression have not been performed. These data are selected because the Doppler estimator is normally applied at this stage in the processing.

Fig. 10 gives the azimuth radiometric gradient of the scene. The land-sea boundaries are clearly seen in the gradient and are one of the main sources of bias in the Doppler estimators. Accordingly, this quality measure is one the best discriminators for this scene, as it is for many scenes. Note that an azimuth AGC effect is seen in the gradient and in the image. This is

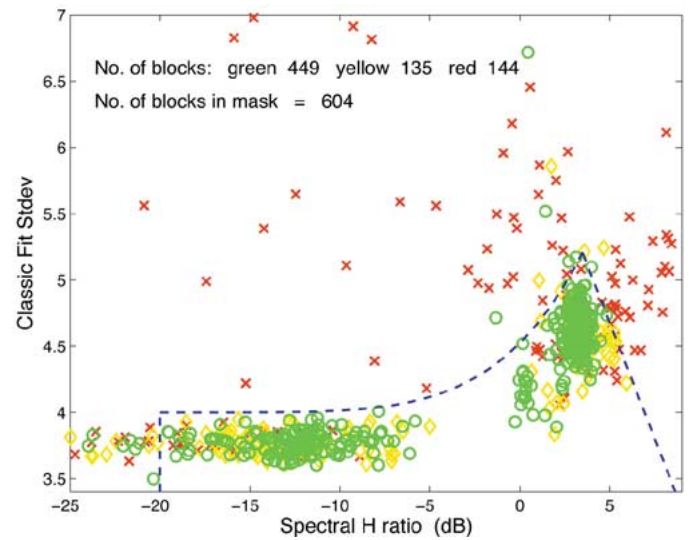


Fig. 12. Scatter plot of "fit standard deviation" in hertz versus SNR.

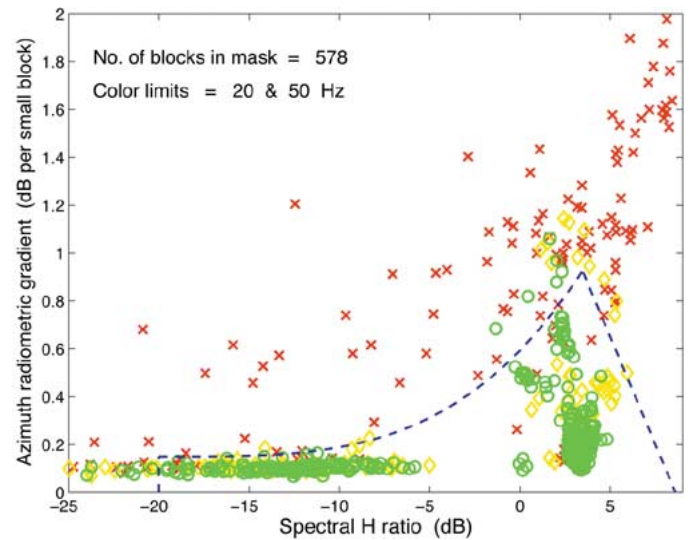


Fig. 13. Scatter plot of azimuth radiometric gradient versus SNR.

normally removed by this stage in the processing, but is left in to further challenge the Doppler estimation algorithms.

A. Block Estimates

The baseband estimator (2) is applied to contiguous 5-km blocks of the scene, and the results are shown in Fig. 11. The baseband estimates are unwrapped assuming a "zero-attitude" slope of Doppler versus range, and the absolute ambiguity level of six PRFs is estimated from the MLBF algorithm and used in (8). It can be seen that the estimates form a consistent pattern, except those on the land-sea boundaries.

B. Examination of Quality Measures

Before the main experiments were performed, the various quality measures discussed in Section II-B were examined, in order to determine their effectiveness and to set suitable thresholds. A Doppler surface fit known to be accurate was used to rate the quality measures. The quality measures were plotted on scatter diagrams, with symbol coding used to indicate whether

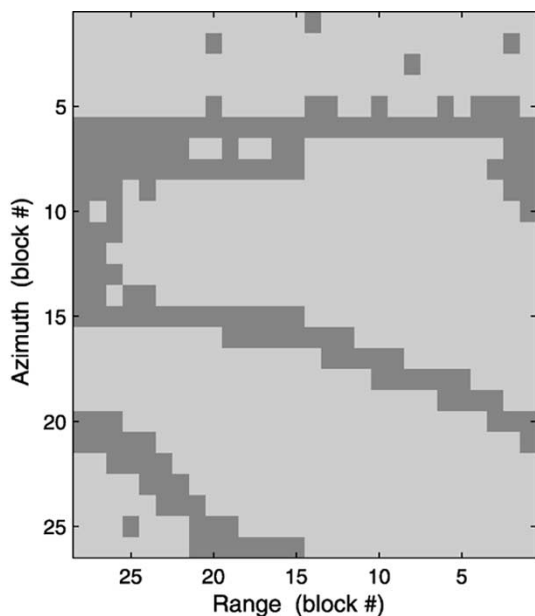


Fig. 14. Mask used in the initial iteration of the automatic surface fit.

the fit deviation of the associated block estimate is less than 20 Hz (shown as green circles), less than 50 Hz (shown with yellow diamonds), or more than 50 Hz (shown by red crosses).

Scatter plots from the Anticosti scene are shown in Figs. 12 and 13, showing the distribution of the standard deviation of the fit and the azimuth radiometric gradient versus SNR. After examining eight scenes from RADARSAT and X-SAR, it is found that these three quality measures provide the best discrimination. The clustering of the good estimates is clearly seen, and thresholds can be selected to effectively separate the blocks that provide accurate estimates from those that provide biased ones.

The thresholds are shown as blue dashed lines in the figures. The clustering boundaries are a little different from one scene to the next, but the performance of the iterative algorithm is sufficiently independent of the location of the boundaries that a single boundary is found to work well for all scenes tested.

The only surprise is provided by the SNR parameter, as measured by the spectral harmonic ratio. It is found that blocks with very low SNRs provide good F_{bb} estimates, as long as the other two quality measures are favorable. Conversely, many blocks with very high SNRs give bad estimates, because they contain strong discrete reflectors that bias the estimates. For this reason, a sloped upper limit is placed on the SNR criterion.

C. Fitting Mask

An initial fitting mask is computed for the Anticosti scene, based on the azimuth radiometric gradient and image SNR, using the thresholds shown in Fig. 13. The resulting mask is shown in Fig. 14, where the dominant effect of the azimuth radiometric gradient of Fig. 10 is seen.

The surface fit algorithm of Section V is run in “automatic” mode on the scene. Selectively chosen termination criteria are used to examine the iterations when many blocks are removed from the fit (44% of the blocks are removed after 132 iterations). The iterations proceed smoothly, but the fitted surface does not change by more than 5 Hz after the first iteration. This suggests

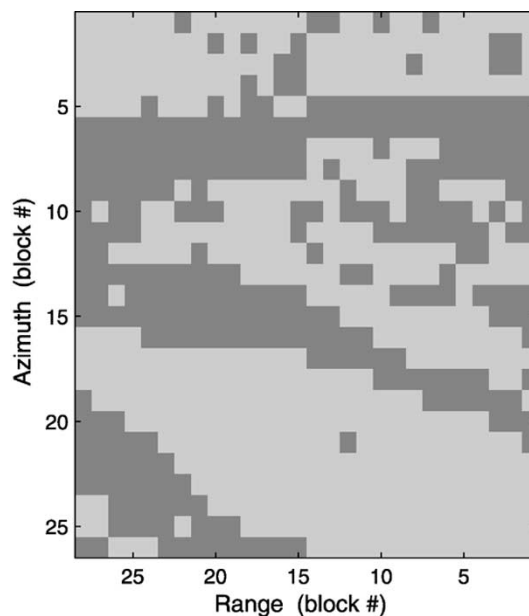


Fig. 15. Mask used in the final iteration of the automatic surface fit.

that quite loose termination criteria can be used, or in some cases the algorithm can be used without resorting to iterations at all.

The final fitting mask is shown in Fig. 15. The additional dark areas on the center right and lower left of the scene are mainly in the water and tend to be removed from the mask relatively late in the iterations. These areas have low SNR, but most of the blocks pass the initial screening of the scatter plots. It is interesting that no single row in the final mask has a full set of good blocks, which indicates the difficulty of fitting polynomials of Doppler versus range for small segments of the image.

D. Fitted Doppler Surface

Fig. 16 gives the final fitted Doppler surface for the Anticosti scene, after the 132 iterations. The estimated values of yaw and pitch and their rates are given in the second column of Table I.

The pitch parameter raises the Doppler frequency more or less uniformly over the whole scene. The yaw parameter increases the Doppler slope between the near and far ranges. The yaw parameter also raises the Doppler over the whole scene, resulting in a high degree of cross coupling between the pitch and yaw parameters, noted earlier. The pitch and yaw rate parameters alter the effect of pitch and yaw as azimuth time advances.

Three other RADARSAT scenes are fitted. The mean and standard deviation of the attitude parameters are given in the third and fourth columns of Table I. Note that biases in the alignment of the antenna or in the attitude control system are absorbed into the estimated pitch and yaw values.

E. Accuracy—Block Deviations

The deviations between the fitted surface and the individual block estimates are shown in Fig. 17. The deviations are less than 7-Hz rms within the blocks used in the fitting mask. Assuming that the estimates within the mask are *unbiased*, the fitted Doppler surface should be accurate to within ± 2 Hz. This is supported by the fact that the fitted surface agrees with the

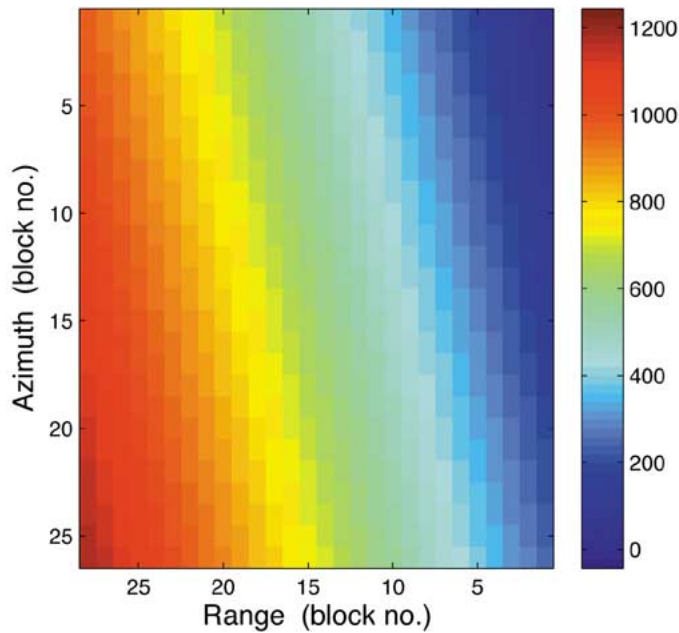


Fig. 16. Fitted Doppler surface (hertz).

TABLE I
PARAMETERS OF AUTOMATIC SURFACE FIT OF ANTICOSTI AND OTHER SCENES

Parameter	Anticosti scene	Mean all scenes	St dev all scenes	Units
Yaw	-0.908	-0.62	0.27	deg
Yaw rate	0.0016	0.0007	0.001	deg/s
Pitch	-0.765	-0.41	0.24	deg
Pitch rate	0.0017	0.0007	0.001	deg/s

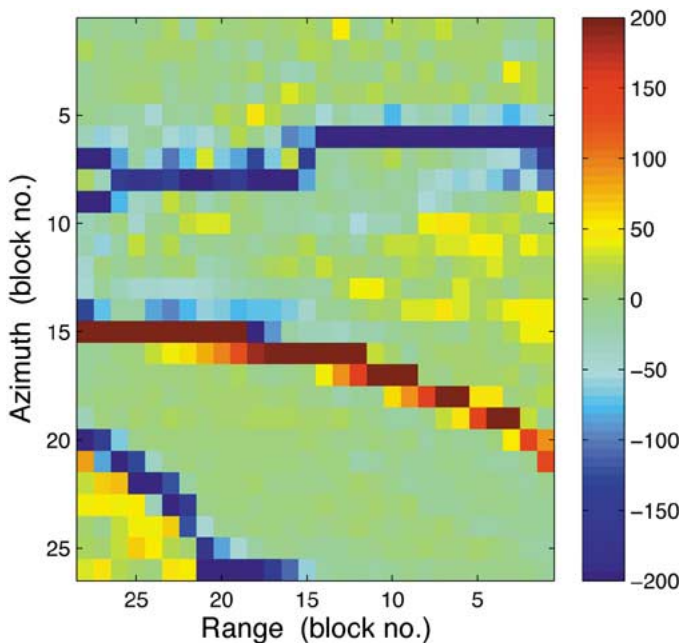


Fig. 17. Deviations between the individual block estimates and the fitted surface (hertz).

best manually obtained fit to within 1 Hz at the four corners of the scene.

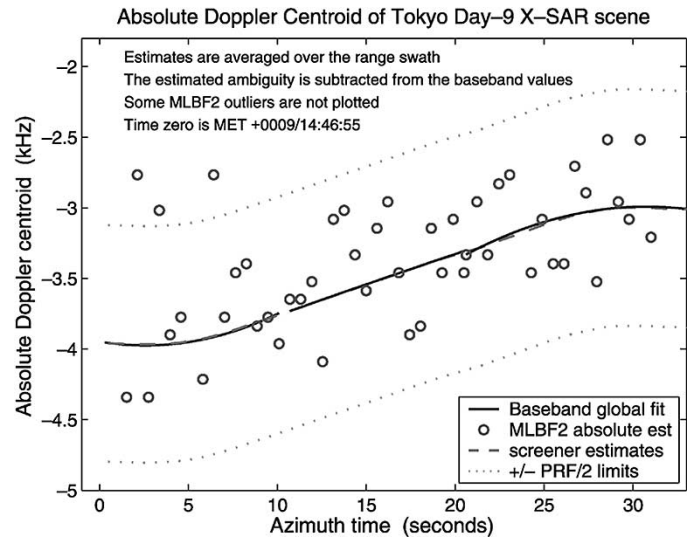


Fig. 18. Doppler estimates from three consecutive frames of an X-SAR scene of the Tokyo area.

VII. SRTM X-SAR RESULTS

Four X-SAR scenes are examined from the February 2000 SRTM mission. The data are taken from the primary antenna and have a higher average SNR than the RADARSAT data. The Doppler centroid is found to vary linearly with time over intervals in the order of 20 s, separated by quadratic changes over about 3 s. The latter is due to the constant angular acceleration produced by the firing of the attitude control thrusters. Because of the high SNR, the Doppler estimation is not difficult, but it is interesting to examine the effect of the thruster firings on the surface fitting procedure.

Three consecutive scenes of the Tokyo area are examined. The results in Fig. 18 show the Doppler estimates versus azimuth time, averaged in the range direction. Attitude thruster firings are occurring between 3 and 6 s and between 26 and 29 s.

The three solid line segments show the fractional Doppler estimates produced by the surface fitting procedure (with the ambiguity added). The estimator has no prior information about the time of the thruster firings. The dashed lines underneath the solid lines show the estimates of the DLR “screener” processor [23], [24], which can be taken as correct (the dashed lines are hidden by the overlaying solid line, except around $t = 24$ s). It can be seen that the quadratic degree of freedom allowed by the surface gives an excellent fit over the first two segments, but overestimates the quadratic component in the third scene, creating errors of up to 15 Hz. This error occurs because the abrupt acceleration of the thrusters causes a transition between the linear and the quadratic parts of the curve, which the model does not allow, except at the edges of the estimation frames. This error would not occur if prior knowledge of the thruster firing times are given to the estimator, or if the scenes are divided at the firing on and off times.

The figure also shows the absolute Doppler estimates produced by the MLBF block estimator. They are shown as small circles, which represent estimates averaged over range. Since 45 out of 55 of the estimates are within $\pm PRF/2$ of the true Doppler

centroid, there is no problem establishing the correct ambiguity number for this scene (the PRF is 1674 Hz).

VIII. CONCLUSION

It is found that SAR scenes often exhibit features that create errors in conventional Doppler estimators. Areas of low SNR, very bright targets, and sharp radiometric gradients are examples that cause difficulties. These areas are typically localized, so the reliability of the estimator can be significantly improved if the offending areas can be identified and selectively removed.

To obtain reliable estimates in the face of such localized disturbances, a new Doppler centroid estimation scheme is developed that embeds the normal estimators in a spatially diverse “global” fitting scheme. Parts of the image that lead to bad estimates are removed on the basis of quality checks, and a wide-area fit of a Doppler “surface” is obtained from the remaining parts.

Two approaches are used to obtain a wide-area surface fit. In one case, a full satellite/earth geometry model is used so that the surface is parameterized using the satellite pitch and yaw and their derivatives. In the second case, a 2-D second-degree polynomial is used to fit the surface. While the full geometry approach is theoretically sounder and imparts a physical reality to the results, it is found that the polynomial model can be just as accurate. The polynomial model is simpler to apply, and physical reality can be imposed by constraints on the polynomial coefficients.

The Doppler centroids of eight RADARSAT-1 and X-SAR SRTM scenes are estimated to test the algorithms. Only a minor amount of sensor-specific tuning is required to optimize the algorithm. The surface fitting approach gives results deemed to be accurate to within a few hertz, even in the face of severe discontinuities in the radiometry, such as land–sea boundaries and areas of low SNR.

The scenes tested are as small as 50 km. However, because of the global fitting approach, the method works even better with larger scenes, including ScanSAR scenes. With larger scenes, the spatial diversity approach is used to better advantage, because larger areas are available to the estimator, even when many bad areas have been removed from the estimation process.

APPENDIX

DETAILS OF THE DOPPLER CALCULATION

The flowchart of the main Doppler frequency calculations is given in Fig. 5. The details of each step in the flow are described in this Appendix. The frames of reference used in the mathematical development are listed in Table II, where the ascending node is assumed to be at the Greenwich meridian. The frames are sketched in Fig. 19, where all “views” are toward the earth’s center from the equator at the Greenwich meridian.

Step 1: Rotate Beam by the Satellite Pitch and Yaw (to Frame 1)

The development begins in the satellite-centered frame of reference, referred to as Frame 0, in which x points up away from the earth’s center, z points “ahead” in the plane of the satellite orbit, perpendicular to x , and y points to the right, completing

TABLE II
CENTER AND ORIENTATION OF FRAMES OF REFERENCE

Frame	Name	Center	Orientation
0	SAT 1	on the satellite	satellite, z forward, x up
1	SAT 2	Earth center	same as Frame 0
2	ECOP	Earth center	orbit plane at ascend. node
3	ECI	Earth center	equator at ascend. node

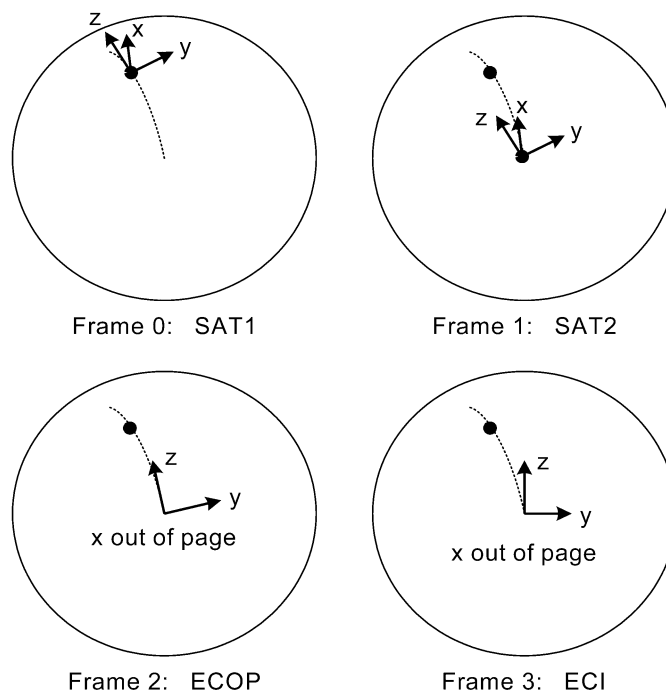


Fig. 19. Frames of reference used in the transformations.

the orthogonal, right-handed frame. For illustration purposes, a circular orbit is assumed, and the satellite position and velocity state vectors are

$$\mathbf{S}_0 = [0 \ 0 \ 0]^T \text{ position} \tag{9}$$

$$\mathbf{V}_0 = [0 \ 0 \ V_{\text{sat}}]^T \text{ velocity} \tag{10}$$

where $V_{\text{sat}} = \sqrt{\mu_e/R_s}$ is the scalar value of the satellite velocity for an orbit of radius R_s , $\mu_e = 3.98601 \times 10^{14}$ is the gravitational constant of the earth, and $[\]^T$ denotes the transpose.³

It is assumed that the radar antenna is attached to the satellite body in such a way that the azimuth boresight lies in the x, y plane for all elevation angles,⁴ and that the specific pointing angle under consideration is defined by the unit view vector

$$\mathbf{U}_{\text{of}} = [-\cos(\alpha) \ \sin(\alpha) \ 0]^T \text{ view vector} \tag{11}$$

³If the orbit is not circular, state vectors can be used, or a vertical component of the velocity can be absorbed into the pitch estimate. If the satellite state vectors S and V are known in ECI or ECR coordinates, they can be used directly in Steps 3 or 4.

⁴If the beam maximum does not lie in this plane, small offsets can be applied to the satellite yaw and pitch estimates to serve as a “calibration” of the antenna boresight alignment.

where α is the “nadir” angle between the local vertical and the beam direction, positive for right-pointing antennas.⁵

Now assume that the satellite is subject to an arbitrary yaw ϕ and pitch ψ . The beam view vector must be rotated using two transformations. First, the view vector is rotated clockwise around the positive y axis by the *pitch angle* ψ , using the Euler transformation matrix [25]⁶

$$\mathbf{T}_{y\psi} = \begin{bmatrix} \cos(\psi) & 0 & \sin(\psi) \\ 0 & 1 & 0 \\ -\sin(\psi) & 0 & \cos(\psi) \end{bmatrix} \quad \begin{array}{l} \text{nose UP} \\ \text{(increases Doppler)} \end{array} \quad (12)$$

Then, the view vector is rotated clockwise around the positive x axis by the *yaw angle* ϕ using the transformation

$$\mathbf{T}_{z\phi} = \begin{bmatrix} 1 & 0 & 0 \\ 0 & \cos(\phi) & -\sin(\phi) \\ 0 & \sin(\phi) & \cos(\phi) \end{bmatrix} \quad \begin{array}{l} \text{nose LEFT} \\ \text{(increases Doppler)} \end{array} \quad (13)$$

so that the unit view vector becomes

$$\mathbf{U}_0 = \mathbf{T}_{x\phi} \mathbf{T}_{y\psi} \mathbf{U}_{0f} \quad (14)$$

in Frame 0.⁷ Finally, this satellite-centered frame is translated to the parallel, earth-centered Frame 1

$$\mathbf{S}_1 = \mathbf{S}_0 + [R_{\text{sat}} \ 0 \ 0]' \quad \text{position} \quad (15)$$

$$\mathbf{V}_1 = \mathbf{V}_0 \quad \text{velocity} \quad (16)$$

$$\mathbf{U}_1 = \mathbf{U}_0 \quad \text{view vector} \quad (17)$$

Step 2: Rotate to ECOP Coordinates (to Frame 2)

Although centered on the earth, the orientation of Frame 1 is aligned with the satellite “zero attitude” direction. As a first step in converting to the ECI reference frame, Frame 1 is rotated “back around the orbit” to the ascending node. The resulting reference system is called the earth-centered orbit plane (ECOP) or Frame 2. If γ_h is the satellite “hour angle” measured from the ascending node crossing, this rotation is clockwise about the y axis for positive γ_h , and is achieved by the transformation matrix

$$\mathbf{T}_{12} = \begin{bmatrix} \cos(\gamma_h) & 0 & -\sin(\gamma_h) \\ 0 & 1 & 0 \\ \sin(\gamma_h) & 0 & \cos(\gamma_h) \end{bmatrix} \quad (18)$$

If the orbit is circular, ω_s is the satellite’s angular rate around its orbit, and if t_s is the time since the ascending node crossing, then $\gamma_h = \omega_s t_s$. Without loss of generality, it can be assumed that the ascending node crossing occurs at longitude zero (the Greenwich meridian).

⁵While the radar beam has an elevation beamwidth of several degrees, only one particular elevation angle is considered at a time, as defined by the “nadir” angle α . Furthermore, it is assumed that the maximum of the symmetrical azimuth beam pattern lies in the (y, z) plane for all nadir angles, in the absence of pitch and yaw, so that the Doppler centroid is the Doppler frequency at this viewing angle.

⁶The conventions for “clockwise” and “counterclockwise” apply when viewing along the axis of rotation in the positive direction. In the current context of a right-pointing antenna, positive pitch and positive yaw each move the right-looking beam forward (“nose up” and “nose left,” respectively, in aircraft terminology). Moving the beam forward *increases* the Doppler centroid frequency.

⁷The order that the transformations are applied (i.e., $\mathbf{T}_{x\phi} \mathbf{T}_{y\psi}$ versus $\mathbf{T}_{y\psi} \mathbf{T}_{x\phi}$) affects the results, but the effect is small for small angles. The correct order is inherent in the *definition* of pitch and yaw.

The ECOP frame corresponds to a view from the equator at the Greenwich meridian, looking into the center of the earth in the direction of the negative x axis. The z axis lies in the orbit plane, and the y axis points to the right, perpendicular to the orbit plane. At $t = 0$, the satellite velocity vector is aligned with the z axis for the circular orbit case. The z axis is inclined counterclockwise from north by the angle κ , which is the inclination angle of the satellite orbit plane, less $\pi/2$.

The transformation of the vectors of interest from Frame 1 to the ECOP Frame 2 is done by the matrix multiplications

$$\mathbf{S}_2 = \mathbf{T}_{12} \mathbf{S}_1 \quad \text{satellite position} \quad (19)$$

$$\mathbf{V}_2 = \mathbf{T}_{12} \mathbf{V}_1 \quad \text{satellite velocity} \quad (20)$$

$$\mathbf{U}_2 = \mathbf{T}_{12} \mathbf{U}_1 \quad \text{view vector} \quad (21)$$

Step 3: Rotate to ECI Coordinates (to Frame 3)

The second step in transforming to the ECI frame of reference is to rotate the ECOP frame clockwise around the x axis by the angle κ . This is achieved by the transformation

$$\mathbf{T}_{23} = \begin{bmatrix} 1 & 0 & 0 \\ 0 & \cos(\kappa) & -\sin(\kappa) \\ 0 & \sin(\kappa) & \cos(\kappa) \end{bmatrix} \quad (22)$$

to obtain

$$\mathbf{S}_3 = \mathbf{T}_{23} \mathbf{S}_2 \quad \text{satellite position} \quad (23)$$

$$\mathbf{V}_3 = \mathbf{T}_{23} \mathbf{V}_2 \quad \text{satellite velocity} \quad (24)$$

$$\mathbf{U}_3 = \mathbf{T}_{23} \mathbf{U}_2 \quad \text{view vector} \quad (25)$$

in Frame 3. This frame corresponds to a “conventional” view of the earth, with z pointing north, y east, and x pointing from the earth’s center to the equator at the Greenwich meridian. The two vectors $(\mathbf{S}_3, \mathbf{V}_3)$ represent the satellite’s state vector, assuming it is expressed in ECI coordinates.⁸

Compensation for Geodetic Latitude: The satellite attitude is often expressed in a frame of reference in which the local vertical is normal to the earth’s ellipsoid, rather than pointing to the earth’s center. This frame is not used in the current development but, nevertheless, the attitude definition can be compensated by adjusting the unit view vector at this point in the transformations.

If $\vartheta_{\text{sat_lat}}$ and $\vartheta_{\text{sat_long}}$ are the latitude and longitude of the satellite, this compensation can be achieved by first rotating the ECI coordinates clockwise around the z axis to the satellite’s longitude using⁹

$$\mathbf{T}_{z3} = \begin{bmatrix} \cos(\vartheta_{\text{sat_long}}) & \sin(\vartheta_{\text{sat_long}}) & 0 \\ -\sin(\vartheta_{\text{sat_long}}) & \cos(\vartheta_{\text{sat_long}}) & 0 \\ 0 & 0 & 1 \end{bmatrix} \quad (26)$$

then tilting the beam slightly toward the equator by the angle

$$\phi_g = \frac{\pi}{180} 0.19242 \sin(2\vartheta_{\text{sat_lat}}) \quad (27)$$

⁸The satellite’s state vector is often expressed in ECR coordinates (as in RADARSAT). Although not used in this analysis, the vectors $(\mathbf{S}_3, \mathbf{V}_3)$ can be converted to ECR coordinates $(\mathbf{S}_4, \mathbf{V}_4)$ by the inverse of the transformation \mathbf{T}_{z43} of (39).

⁹Satellite latitude is geocentric and positive in the Northern Hemisphere; satellite longitude is positive to the east of the Greenwich meridian.

using the transformation

$$\mathbf{T}_{y3} = \begin{bmatrix} \cos(\phi_g) & 0 & -\sin(\phi_g) \\ 0 & 1 & 0 \\ \sin(\phi_g) & 0 & \cos(\phi_g) \end{bmatrix} \quad (28)$$

then rotating back around the z axis to ECI coordinates using \mathbf{T}_{z3}^{-1} . The net result is

$$\mathbf{U}_{3g} = \mathbf{T}_{z3}^{-1} \mathbf{T}_{y3} \mathbf{T}_{z3} \mathbf{U}_3 \quad \text{view vector} \quad (29)$$

Note that the compensation angle ϕ_g is zero at the equator and the poles, and has a maximum of 0.19242° at $\pm 45^\circ$ latitude. The formula (27) is an approximation that is accurate to within 0.0003° [because the compensation is small, it does not matter if $\vartheta_{\text{sat_lat}}$ is expressed in circular or geodetic latitude units in (27)]. The effect of the transformation (29) is to rotate the view vector so that the satellite pitch and yaw, which is originally specified with respect to the local horizontal, is correct in the ECI frame.

Step 4: Solve for the Target Location

The next step is to locate the target on the earth's surface, by finding the intersection of the current beam direction with the earth's surface. The surface is defined by the WGS-84 ellipsoid, but if the local terrain height is known, the ellipsoid can be adjusted. The WGS-84 ellipsoid has an ellipticity

$$\epsilon = \frac{A_e^2 - B_e^2}{B_e^2} \quad (30)$$

where $A_e = 6378137.0$ and $B_e = 6356752.3142$ are the equatorial and polar radii in meters. The geometry is solved by finding the smallest root of the quadratic equation

$$R_3^2 + 2FR_3 + G = 0 \quad (31)$$

with the coefficients

$$F = \frac{\mathbf{S}_3 \bullet \mathbf{U}_{3g} + \epsilon S_3(x) U_{3g}(x)}{1 + \epsilon U_{3g}^2(x)} \quad (32)$$

$$G = \frac{\mathbf{S}_3 \bullet \mathbf{S}_3 - A_e^2 + \epsilon S_3^2(x)}{1 + \epsilon U_{3g}^2(x)} \quad (33)$$

where \bullet is the dot product, and $S_3(z)$ is the z component of \mathbf{S}_3 from (23). The scalar variable R_3 is the range from the satellite to the target on the earth's surface, found by solving (31)

$$R_3 = -F - \sqrt{F^2 - G} \quad \text{slant range to target.} \quad (34)$$

Having found the *range* to the target, the *location* of the target in ECI coordinates can be found by extrapolating by this distance along the view vector, \mathbf{U}_{3g} , starting from the satellite position. The resulting target position is

$$P_3 = S_3 + R_3 \mathbf{U}_{3g} \quad \text{target position.} \quad (35)$$

Step 5: Find the Target Velocity

The target's velocity must now be found in the ECI coordinates. The target is assumed to be stationary with respect to the earth's surface, but if it is not stationary, a suitable component can be included in (37). The magnitude of the velocity is a function of the target's latitude and the direction of the velocity is

a function of the target's longitude. The target rotates with the earth around the polar axis, with a radius

$$D_3 = \sqrt{P_3^2(y) + P_3^2(x)} \quad (36)$$

so that the target's velocity vector is

$$\mathbf{Q}_3 \mathbf{r} = [0 \quad D_3 \omega_e \quad 0]' \quad (37)$$

in ECR coordinates, where $\omega_e = 7.2921 \times 10^{-5}$ is the earth's rotation rate in an inertial reference frame. To get the target velocity into the standard ECI coordinates of Frame 3, it must be rotated about the polar axis z by the target ECI longitude

$$\vartheta_{\text{tar_long}} = \arctan \{P_3(y), P_3(x)\} \quad (38)$$

using the transformation

$$\mathbf{T}_{z43} = \begin{bmatrix} \cos(\vartheta_{\text{tar_long}}) & -\sin(\vartheta_{\text{tar_long}}) & 0 \\ \sin(\vartheta_{\text{tar_long}}) & \cos(\vartheta_{\text{tar_long}}) & 0 \\ 0 & 0 & 1 \end{bmatrix}. \quad (39)$$

This gives the target velocity in ECI coordinates

$$\mathbf{Q}_3 = \mathbf{T}_{z43} \mathbf{Q}_4 \mathbf{r} \quad \text{target velocity.} \quad (40)$$

Step 6: Calculate the Doppler Frequency

To calculate the target's Doppler frequency, the relative velocity of the satellite, with respect to the target, must be found. This is done by projecting each of the velocities along the radar view vector and subtracting them. This projection can be done in either the ECI or ECR frames. In the ECI frame, the relative velocity is obtained from

$$\mathbf{V}_{\text{rel}} = \mathbf{V}_3 \bullet \mathbf{U}_{3g} - \mathbf{Q}_3 \bullet \mathbf{U}_{3g} = (\mathbf{V}_3 - \mathbf{Q}_3) \bullet \mathbf{U}_{3g}. \quad (41)$$

The Doppler frequency of the target in the center of the beam (the Doppler centroid) is then

$$F_d = -\frac{2V_{\text{rel}}}{\lambda} \quad (42)$$

where λ is the radar wavelength.

ACKNOWLEDGMENT

The author is grateful to R. Bamler and the staff of the German Remote Sensing Data Center at DLR for hosting the author during his sabbatical year and for providing data and advice on the current work. The author would like to acknowledge the helpful advice of B. Hawkins (Canada Centre for Remote Sensing), who also provided the RADARSAT data for the study. The author is also grateful to K. Magnussen, B. Robertson, and F. Wong (MacDonald Dettwiler), who provided help in formulating the geometry model.

REFERENCES

- [1] I. G. Cumming and J. R. Bennett, "Digital processing of SEASAT SAR data," in *Rec. IEEE Int. Conf. Acoustics, Speech Signal Processing*, Washington, D.C., Apr. 1979, pp. 710–718.
- [2] J. C. Curlander, C. Wu, and A. Pang, "Automatic preprocessing of spaceborne SAR data," in *Proc. IGARSS*, vol. 3, Munich, June 1–4, 1982, pp. 1–6.
- [3] F. K. Li, D. N. Held, J. Curlander, and C. Wu, "Doppler parameter estimation for spaceborne synthetic aperture radars," *IEEE Trans. Geosci. Remote Sensing*, vol. GE-23, pp. 47–56, Jan. 1985.
- [4] J. Curlander and R. McDonough, *Synthetic Aperture Radar: Systems and Signal Processing*. New York: Wiley, 1991.

- [5] D. E. Fernandez, P. J. Meadows, B. Schaeftler, and P. Mancini, "ERS attitude errors and its impact on the processing of SAR data," in *Proc. CEOS SAR Workshop*, Toulouse, France, Oct. 26–29, 1999. Online. [Available]: <http://www.estec.esa.nl/ceos99/papers/p027.pdf>.
- [6] M. Y. Jin, "Optimal range and Doppler centroid estimation for a ScanSAR system," *IEEE Trans. Geosci. Remote Sensing*, vol. 34, pp. 479–488, Mar. 1996.
- [7] —, "Optimal Doppler centroid estimation for SAR data from a quasihomogeneous source," *IEEE Trans. Geosci. Remote Sensing*, vol. GE-24, pp. 1022–1025, 1986.
- [8] S. N. Madsen, "Estimating the Doppler centroid of SAR data," *IEEE Trans. Aerosp. Electron. Syst.*, vol. 25, pp. 135–140, Mar. 1989.
- [9] M. Dragošević, "On accuracy of attitude estimation and Doppler tracking," in *Proc. CEOS SAR Workshop*, Toulouse, France, Oct. 26–29, 1999. Online. [Available]: <http://www.estec.esa.nl/ceos99/papers/p164.pdf>.
- [10] M. Dragošević and B. Plache, "Doppler tracker for a spaceborne ScanSAR system," *IEEE Trans. Aerosp. Electron. Syst.*, vol. 36, pp. 907–924, July 2000.
- [11] F.-K. Li and W. T. K. Johnson, "Ambiguities in spaceborne SAR systems," *IEEE Trans. Aerosp. Electron. Syst.*, vol. AE-19, May 1983.
- [12] I. G. Cumming, P. F. Kavanagh, and M. R. Ito, "Resolving the Doppler ambiguity for spaceborne synthetic aperture radar," in *Proc. IGARSS*, Zurich, Switzerland, Sept. 8–11, 1986, pp. 1639–1643.
- [13] C. Y. Chang and J. C. Curlander, "Doppler centroid ambiguity estimation for synthetic aperture radars," in *Proc. IGARSS*, Vancouver, BC, Canada, 1989, pp. 2567–2571.
- [14] —, "Applications of the multiple PRF technique to resolve Doppler centroid estimation ambiguity for spaceborne SAR," *IEEE Trans. Geosci. Remote Sensing*, vol. 30, pp. 941–949, Sept. 1992.
- [15] R. Bamler and H. Runge, "PRF ambiguity resolving by wavelength diversity," *IEEE Trans. Geosci. Remote Sensing*, vol. 29, pp. 997–1003, Nov. 1991.
- [16] F. H. Wong and I. G. Cumming, "A combined SAR Doppler centroid estimation scheme based upon signal phase," *IEEE Trans. Geosci. Remote Sensing*, vol. 34, pp. 696–707, May 1996.
- [17] C. S. Purry, K. Dumper, G. C. Verwey, and S. R. Pennock, "Resolving Doppler ambiguity for ScanSAR data," in *Proc. IGARSS*, vol. 5, Honolulu, HI, July 24–28, 2000, pp. 2272–2274.
- [18] J. A. Nelder and R. Mead, "A simplex method for function minimization," *Comput. J.*, vol. 7, pp. 308–313, 1965.
- [19] O. Loffeld, "Estimating time varying Doppler centroids with Kalman filters," in *Proc. IGARSS*, vol. 2, Helsinki, Finland, June 3–6, 1991, pp. 1059–1063.
- [20] S. R. Marandi, "RADARSAT attitude estimates based on Doppler centroid of satellite imagery," in *Proc. IGARSS*, vol. 1, Singapore, Aug. 3–8, 1997, pp. 493–497.
- [21] J. B.-Y. Tsui, *Fundamentals of Global Positioning System Receivers, A Software Approach*. New York: Wiley, 2000.
- [22] R. K. Raney, "Doppler properties of radars in circular orbits," *Int. J. Remote Sens.*, vol. 7, no. 9, pp. 1153–1162, 1986.
- [23] U. Steinbrecher, R. Bamler, M. Eineder, and H. Breit, "SRTM data quality analysis," in *Proc. 3rd Eur. Conf. Synthetic Aperture Radar, EUSAR 2000, VDE*, München, Germany, May 23–25, 2000, pp. 217–218.
- [24] A. Roth, M. Eineder, B. Rabus, E. Mikusch, and B. Schattler, "SRTM/X-SAR: Products and processing facility," in *Proc. IGARSS*, vol. 2, Sydney, July 2001, pp. 745–747.
- [25] I. M. Yaglom, I. M. Yaglom, and A. Shields, *Geometric Transformations: Math. Assoc. Amer.*, 1962.



Ian G. Cumming (S'63–M'66) received the B.Sc. degree in engineering physics from the University of Toronto, Toronto, ON, Canada, in 1961, and the Ph.D. degree in computing and automation from Imperial College, University of London, London, U.K., in 1968.

He joined MacDonald, Dettwiler and Associates, Ltd., Richmond, BC, Canada, in 1977, and since that time, he has developed synthetic aperture radar signal processing algorithms, including Doppler estimation and autofocus. He has been involved in the algorithm design of the digital SAR processors for SEASAT, SIR-B, ERS-1/2, J-ERS-1, and RADARSAT, as well as several airborne radar systems. He has also worked on systems for processing polarimetric and interferometric radar data, and the compression of radar data. In 1993, he joined the Department of Electrical and Computer Engineering, University of British Columbia, Vancouver, BC, Canada, where he holds the MacDonald Dettwiler/NSERC Industrial Research Chair in Radar Remote Sensing. The Radar Remote Sensing laboratory supports a research staff of eight engineers and students, working in the fields of SAR processing, SAR data encoding, satellite SAR two-pass interferometry, airborne along-track interferometry, airborne polarimetric radar classification, and SAR Doppler estimation.